PHYSICAL REVIEW A **96**, 043426 (2017)

Control of three-dimensional electron vortices from femtosecond multiphoton ionization

D. Pengel, S. Kerbstadt, L. Englert, T. Bayer, and M. Wollenhaupt
Carl von Ossietzky Universität Oldenburg, Institut für Physik, Carl-von-Ossietzky-Straße 9-11, D-26129 Oldenburg, Germany

(Received 18 September 2017; published 31 October 2017)

We report on the creation and manipulation of three-dimensional (3D) electron vortices from femtosecond multiphoton ionization of atoms. Vortex-shaped photoelectron momentum distributions arise from the superposition of two time-delayed free-electron wave packets with different magnetic quantum numbers. In the experiment, pairs of time-delayed counter-rotating circularly polarized (CRCP) femtosecond laser pulses, generated from a polarization-shaped supercontinuum source, are used to ionize potassium atoms. The resulting 3D electron vortices are reconstructed tomographically from a set of velocity map imaging measurements. By variation of the time delay, the helicity, and the spectral bandwidth of the CRCP pulse sequence, we control the radial vortex shape. Absorption of another photon in the continuum changes the c_6 azimuthal symmetry of the threshold vortex into c_8 for above-threshold ionization. Electron vortices from nonperturbative excitation show c_4 azimuthal symmetry and a π-phase jump in the polar direction. Determination of the relative phase of the superposition state allows us to reconstruct a free-electron wave function.

DOI: 10.1103/PhysRevA.96.043426

I. INTRODUCTION

Vortices are a ubiquitous phenomenon in physics. Their structures and dynamics are studied in diverse fields including meteorology [1], fluid mechanics [2], optics [3,4], nanoplasmonics [5], and superfluidity [6] down to the quantum regime of atomic-scale wave functions [7–10]. Recently, the emergence of vortex structures in the momentum distribution of free-electron wave packets from the photoionization of atoms with sequences of two time-delayed counter-rotating circularly polarized (CRCP) ultrashort laser pulses was predicted [11] and demonstrated experimentally [12]. In subsequent theoretical studies, the generation of multi-arm electron vortices by photoionization of atoms [13] and molecular ions [14,15] in circularly polarized bichromatic laser fields [16] was investigated. Here, we extend the work reported in [12] and present an experimental study of the creation and manipulation of electron vortices by resonance-enhanced multiphoton ionization (REMPI) of atoms using femtosecond CRCP pulse sequences.

In general, the photoionization of atoms with circularly polarized (CP) pulse sequences has recently attracted a great deal of attention. For example, CRCP pulse sequences with adjustable temporal overlap are routinely used in high harmonic generation to produce isolated attosecond pulses by polarization gating [17–19]. In strong-field ionization, an asymmetry between the ionization yields from CRCP and corotating CP (COCP) laser pulse sequences was predicted theoretically [20] and confirmed experimentally in the tunneling [21] and multiphoton [22] regimes. In multiphoton ionization of potassium atoms, specific polarization-shaped femtosecond laser pulses containing a sequence of right- (RCP) and left-handed circularly polarized (LCP) subpulses have been studied for coherent control of photoelectron angular interferograms [23].

Photoelectron vortices arise from the interference of two time-delayed free-electron wave packets with different magnetic quantum numbers m. Besides their aesthetic properties [24], vortex-shaped free-electron wave packets are prototype examples of highly phase-sensitive coherent superposition states. As such, they represent ideal test beds to study the physical mechanisms of coherent control based on photoinduced multipath interference. Interfering target states with the same energy E, excited via M- and N-photon pathways from the ground state, will have either equal or opposite parity depending on the number of absorbed photons M and N. It was pointed out [25] that opposite parity allows for control of the angular distribution of the final coherent superposition state and, hence, to steer the directionality of the quantum dynamics [26–30]. However, in addition, excitation to target states with the same parity permits control over the angular distribution of the final state. The electron vortices reported in this paper are generated by 1+2 REMPI of potassium atoms and thus are representative of the latter category with $M = N = 3$. The distinct spiral-shaped angular distribution of the final-state wave packet is obtained by photoionization into different angular momentum states in the continuum. For ionization, we employ pairs of counter-rotating femtosecond pulses either from an amplified femtosecond laser system or an ultrabroadband white-light supercontinuum source. We demonstrate control over the vortex shape in the radial direction by variation of the spectral bandwidth, the time delay, and the helicity of the laser pulses. In particular, the use of ultrabroadband pulses allows us to observe a "full six-arm vortex," i.e., an electron wave packet with c_6 rotational symmetry spanning an ultrabroad range of photoelectron kinetic energies down to zero kinetic energy. Furthermore, the use of these few-cycle supercontinuum laser pulses allows us to reduce the time delays to 10 fs, which enables high-resolution measurement of the radial interference fringes. In addition, we demonstrate electron vortices with different rotational symmetries. Absorption of an additional photon in the continuum produces vortices in the above-threshold ionization (ATI) with c_8 rotational symmetry, whereas four-arm electron vortices are observed for nonperturbative π-pulse excitation [12]. Finally, by evaluation of the relative phase of the interfering wave packets, we reconstruct the quantum mechanical wave function of a free-electron wave packet.

The paper is organized as follows. We start in Sec. II with a consistent physical description for the generation

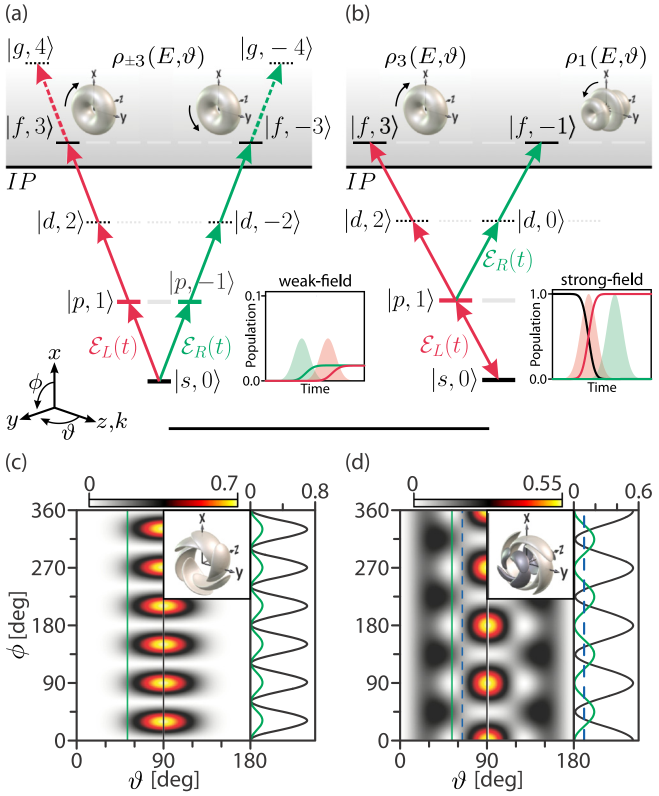

FIG. 1. Excitation and ionization schemes of potassium atoms interacting with CRCP pulse sequences. (a) In the perturbative regime, 1+2 REMPI using an RLCP sequence launches an $|f,-3\rangle$ and a time-delayed $|f,3\rangle$ free-electron wave packet. Interference of the two wave packets yields a counterclockwise rotating electron vortex with c_6 rotational symmetry. Analogously, interference of time-delayed $|g,\pm4\rangle$ wave packets created by ATI gives rise to an eight-arm vortex. (b) Population inversion in the resonant $4s$-$4p$ system using LRCP π pulses opens routes to an $|f,-1\rangle$ and a $|p,-1\rangle$ (not shown) continuum. Interference of the former with the $|f,3\rangle$ wave packet results in a clockwise-rotating electron vortex with c_4 symmetry. The additional $|p,-1\rangle$ contribution leads to variations of the vortex in the ϑ direction (see Sec. IV B 3). (c), (d) Calculated interference terms of the corresponding photoelectron densities on a sphere with fixed energy E_0. Vertical lines indicate sections along the ϕ direction plotted in the right-hand frames.

of all electron vortices (c_4, c_6, and c_8). In Sec. III, we describe our experimental techniques comprised of white-light polarization shaping and photoelectron imaging tomography. The experimental results are presented in Sec. IV, where Sec. IV A is dedicated to control of the radial vortex shape and in Sec. IV B we demonstrate manipulation of the angular vortex shape in both the azimuthal and polar directions. Section V concludes the paper with a brief summary and outlook.

II. THEORY

The physical mechanism underlying the creation of free-electron vortices is based on the superposition of two time-delayed photoelectron wave packets with different magnetic quantum number m [11,12]. In our experiment, those electron wave packets are generated by 1+2 REMPI of ground-state potassium atoms with a sequence of two phase-locked time-delayed CRCP femtosecond laser pulses. The corresponding excitation scheme is depicted in Fig. 1. Owing to the selection rules $\Delta l = \pm1$ and $\Delta m = \pm1$ for $\sigma^{\pm}$ transitions, perturbative ionization occurs essentially along two ionization pathways. The right-handed CP (RCP) laser pulse $\mathcal{E}_R(t)$ ionizes the atom via the $\Delta l = 1$ and $\Delta m = -1$ pathway, whereas the left-handed CP (LCP) pulse $\mathcal{E}_L(t)$ drives the excitation along the $\Delta l = 1$ and $\Delta m = 1$ pathway. If the two pulses do not overlap in time, $\Delta l = -1$ pathways are suppressed due to the increasing $|m|$ value in the nonresonant two-photon ionization step. Therefore, perturbative 1+2 REMPI with CP pulses connects the $4s$ ground state to an f-type continuum, as depicted in Fig. 1(a) for the example of an RCP pulse preceding an LCP pulse, i.e., an RLCP pulse sequence. In the discussion below, the RLCP pulse ordering corresponds to positive time delay, $\tau > 0$, while the LRCP configuration, where the RCP pulse follows the LCP pulse, corresponds to $\tau < 0$. In Fig. 1(a), the first RCP pulse ionizes the atom via the three-photon route, $|s,0\rangle \xrightarrow{\mathcal{E}_R} |p,-1\rangle \xrightarrow{\mathcal{E}_R} |d,-2\rangle \xrightarrow{\mathcal{E}_R} |f,-3\rangle$, and creates a torus-shaped free-electron wave packet. The wave function can be written as

$$\psi_{f,-3}(E,\vartheta,\phi) = \mathcal{R}_3(E)\, Y_{3,-3}(\vartheta,\phi), \tag{1}$$

where the radial part $\mathcal{R}_3(E)$ describes the photoelectron kinetic-energy distribution. In general, for nonresonant perturbative N-photon ionization, $\mathcal{R}_N(E)$ is related to the Nth-order spectrum of the ionizing laser pulse [31,32]. The angular part is given by the spherical harmonic $Y_{l,m}(\vartheta,\phi) = P_{l,m}(\vartheta)e^{im\phi}$ (see Fig. 1 for definition of the angles ϑ and ϕ), with the polar part $P_{l,m}(\vartheta)$ being proportional to the associated Legendre polynomial $P_l^{(m)}[\cos(\vartheta)]$. The second LCP pulse ionizes the atom via the three-photon route, $|s,0\rangle \xrightarrow{\mathcal{E}_L} |p,1\rangle \xrightarrow{\mathcal{E}_L} |d,2\rangle \xrightarrow{\mathcal{E}_L} |f,3\rangle$. Analogously, the resulting photoelectron wave packet is described by the wave function

$$\psi_{f,3}(E,\vartheta,\phi) = \mathcal{R}_3(E)\, Y_{3,3}(\vartheta,\phi). \tag{2}$$

Due to the time delay τ between the two pulses, the wave packet launched by the first pulse acquires the quantum mechanical time-evolution phase of $e^{-iE\tau/\hbar}$. Thus, the final superposition state reads

$$\begin{aligned}\Psi_6(E,\vartheta,\phi) &= \psi_{f,-3}(E,\vartheta,\phi)e^{-iE\tau/\hbar} + \psi_{f,3}(E,\vartheta,\phi)\\ &= \mathcal{R}_3(E)P_{3,-3}(\vartheta)(e^{-i(3\phi+E\tau/\hbar)} - e^{i3\phi}).\end{aligned} \tag{3}$$

The minus sign in the second term results from the symmetry relation $Y_{l,-m}(\vartheta,\phi) = (-1)^m\, Y^*_{l,m}(\vartheta,\phi)$ of the spherical harmonics. The index "6" of the total wave function refers to its c_6 rotational symmetry (see discussion below). The probability density of the photoelectron is given by the absolute square,

$$|\Psi_6(E,\vartheta,\phi)|^2 = 2\rho_3(E,\vartheta)[1 - \cos(6\phi + E\tau/\hbar)]. \tag{4}$$

This expression describes the final-state density as a product of the torus-shaped wave packet $\rho_3(E,\vartheta) = |\psi_{f,\pm3}(E,\vartheta,\phi)|^2$ created by each individual pulse and an interference term in the form of an Archimedean spiral. In general, Archimedean spirals are defined by linear progression of the isophase contour lines in the polar plane, i.e., the ϕ-E plane: $E_{iso}(\phi) = a\phi + c$. Considering the argument of the cosine function in

Eq. (4), we find, for the nth maximum (arm) of the spiral,

$$E_n(\phi) = -\frac{6\hbar}{\tau}\phi + \frac{(2n+1)\pi\hbar}{\tau}, \tag{5}$$

with $\phi < 0$ chosen such that $E_n(\phi) \geqslant 0$ and $E_n(\phi_0) = 0$ for the initial angle ϕ_0 defining the start of the spiral arm. From Eq. (5), we infer three different attributes characterizing the electron vortex. First, the energetic separation of adjacent vortex arms is $\delta E = E_{n+1}(\phi) - E_n(\phi) = h/\tau$ and can thus be precisely tuned by the time delay in the pulse sequence. Second, the azimuthal separation of adjacent vortex arms is $\delta\phi = \phi_{n+1}(E) - \phi_n(E) = 2\pi/6$, implying c_6 rotational symmetry of the total vortex-shaped wave function. Lastly, the negative slope $E'(\phi)$ of the spiral arms for $\tau > 0$ defines counterclockwise rotation of the vortex [12]. The rotational sense is reversed by changing the sign of τ, i.e., by reversal of the pulse ordering. Using a negative time delay $\tau < 0$ results in an LRCP pulse sequence which creates a vortex-shaped wave packet with clockwise sense of rotation.

Next, we consider the case of ATI, as indicated by the dashed arrows in Fig. 1(a). Absorption of an additional photon in the ionization continuum generates electron wave packets with kinetic energy $\hbar\omega_0$ above the threshold signal, where ω_0 denotes the laser central frequency. In analogy to the above discussion, ATI via the four-photon routes $|s,0\rangle \xrightarrow{\mathcal{E}_{R/L}} |p,\mp1\rangle \xrightarrow{\mathcal{E}_{R/L}} |d,\mp2\rangle \xrightarrow{\mathcal{E}_{R/L}} |f,\mp3\rangle \xrightarrow{\mathcal{E}_{R/L}} |g,\mp4\rangle$ using an RLCP pulse sequence yields the final-state photoelectron wave function,

$$\Psi_8(E,\vartheta,\phi) = \mathcal{R}_4(E)P_{4,4}(\vartheta)\left(e^{-i(4\phi+E\tau/\hbar)} + e^{i4\phi}\right). \tag{6}$$

The corresponding density reads

$$|\Psi_8(E,\vartheta,\phi)|^2 = 2\rho_4(E,\vartheta)[1+\cos(8\phi+E\tau/\hbar)], \tag{7}$$

with $\rho_4(E,\vartheta) = |\psi_{g,\pm4}(E,\vartheta,\phi)|^2$ describing a g-type torus. Comparison of Eqs. (7) and (4) suggests that the final-state wave packet from ATI exhibits c_8 rotational symmetry corresponding to an eight-arm electron vortex. In general, the number of arms n_a of an electron vortex resulting from the interference of an M- and an N-photon route from the same initial state is given by

$$n_a = \Delta m_1 M - \Delta m_2 N, \tag{8}$$

where Δm_1 and Δm_2 are the helicities of the first and second pulse, respectively.

Figure 1(b) displays nonperturbative excitation of the atom by an LRCP sequence ($\tau < 0$). Both pulses have a pulse area of π with respect to the resonant $4s \rightarrow 4p$ transition—briefly termed π pulses in the following. The first LCP π pulse steers the atom into the resonant $|p,1\rangle$ state [see inset to Fig. 1(b)] and simultaneously drives perturbative 1+2 REMPI creating an $|f,3\rangle$ free-electron wave packet [cf. Eq. (2)]. The inversion induced by the first π pulse alters the initial conditions for the second. Finding the atom in the excited $4p$ state, the second pulse ionizes the atom along the two-photon route, $|p,1\rangle \xrightarrow{\mathcal{E}_R} |d,0\rangle \xrightarrow{\mathcal{E}_R} |f,-1\rangle$, and creates the free-electron wave packet,

$$\psi_{f,-1}(E,\vartheta,\phi) = \mathcal{R}_3(E)P_{3,-1}(\vartheta)e^{-i\phi}. \tag{9}$$

The corresponding density $\rho_1(E,\vartheta) = |\psi_{f,-1}(E,\vartheta,\phi)|^2$ is illustrated in the top-right corner of Fig. 1(b). Note that in this case, $\Delta l = -1$ transitions, e.g., ionization via the two-photon route $|p,1\rangle \xrightarrow{\mathcal{E}_R} |s,0\rangle \xrightarrow{\mathcal{E}_R} |p,-1\rangle$, are allowed as well. Hence, in a complete description, contributions from a p-type continuum need to be considered in addition. For simplicity, we focus on the f-type wave packets in the discussion below. However, signatures of the p-type wave packets are indeed observed in the experiment and will be discussed in Sec. IV B 2. Coherent superposition of the $|f,3\rangle$ and the $|f,-1\rangle$ wave packets in Eqs. (2) and (9) gives rise to the total photoelectron distribution,

$$\begin{aligned}|\Psi_4(E,\vartheta,\phi)|^2 &= [\rho_1(E,\vartheta)+\rho_3(E,\vartheta)]\\ &\quad\times[1 - A(\vartheta)\cos(4\phi - E\tau/\hbar)],\end{aligned} \tag{10}$$

with $A(\vartheta) = 2P_{3,1}(\vartheta)P_{3,3}(\vartheta)/[P^2_{3,1}(\vartheta)+P^2_{3,3}(\vartheta)]$. In this case, the cosine function describes a clockwise-rotating Archimedean spiral with c_4 rotational symmetry. This result is in accordance with Eq. (8), which predicts an $n_a = 4$-arm electron vortex for ionization starting from the $|p,1\rangle$ state. Unlike the perturbative vortices in Eqs. (4) and (7), however, the spiral structure of the nonperturbative vortex in Eq. (10) is modulated in the polar direction by the function $A(\vartheta)$. This modulation also has important consequences for the vortex shape in the ϕ direction.

The differences between the nonperturbative four-arm vortex in Eq. (10) and the perturbative six-arm vortex in Eq. (4) are most clearly seen in a spherical representation. Figures 1(c) and 1(d) display the corresponding interference terms as a function of the angles ϑ and ϕ for fixed photoelectron energy E_0. Along the ϕ direction, both plots reflect the rotational symmetry of the respective vortices, that is, c_6 in the perturbative and c_4 in the nonperturbative case. Sections in the azimuthal direction taken at $\vartheta = 90^\circ$ (x-y plane), shown as black curves in the right-hand frames, display clear sixfold and fourfold periodicity, respectively. Here, in the laser polarization plane, Eqs. (10) and (4) are fully analogous due to $A(90^\circ) \approx 1$. In the perturbative case, variation of ϑ leads to a monotonous decay of the signal, as indicated by the section taken at $\vartheta = 55^\circ$ and plotted as a green curve in Fig. 1(c). In contrast, in the nonperturbative case, the vortex structure undergoes a distinct phase shift of π at $\vartheta = 63^\circ$ before fading, as highlighted by the green curve taken at $\vartheta = 55^\circ$ in Fig. 1(d). In the transition region around $\vartheta = 63^\circ$, the ϕ dependence of the wave packet vanishes and the vortex structure is smoothed out [blue dashed curve in Fig. 1(d)]. This π jump in the vortex phase is induced by the node of the $|f,-1\rangle$ wave function, which inverts the relative phase between the interfering wave packets $|f,-1\rangle$ and $|f,3\rangle$. Measurement of this phase shift provides a method to determine the free-electron wave function, rather than its probability density (see Sec. IV B 2).

III. SETUP

The experimental setup is depicted in Fig. 2. CRCP pulse sequences are generated using a home-built $4f$ polarization pulse shaper equipped with a dual-display liquid-crystal spatial-light modulator (LC-SLM; Jenoptik SLM-640d) [16,33–35]. The p-polarized input pulses with central wavelength $\lambda_0 = 790$ nm and a full width at half maximum of $\Delta\lambda = 80$ nm are provided by a multipass chirped-pulse

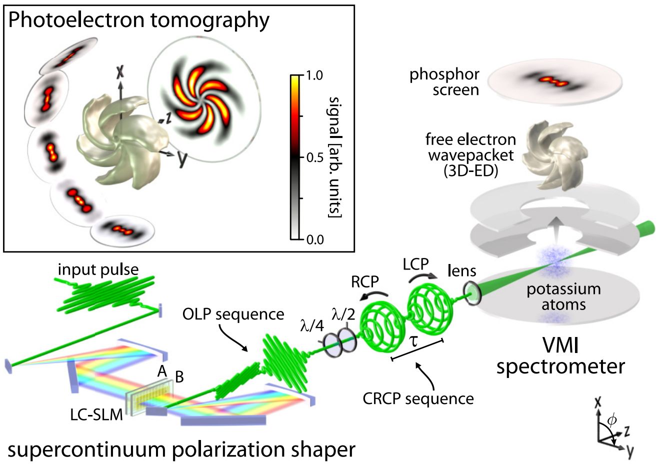

FIG. 2. Experimental setup. A $4f$ supercontinuum polarization shaper is used to generate an OLP pulse sequence of variable time delay τ by linear spectral phase modulation. The OLP sequence is converted into a rotatable CRCP sequence (here LRCP) using a QWP ($\lambda/4$) followed by a HWP ($\lambda/2$). Free-electron wave packets created by the multiphoton ionization of potassium atoms are imaged by a VMI spectrometer. By rotation of the HWP, we measure images of the free-electron wave packet under different angles, as illustrated in the inset, and reconstruct the 3D-ED using a tomographic algorithm.

amplifier (Femtolasers Femtopower HR 3 kHz seeded by a Rainbow 500 oscillator). For the experiments based on an over octave-spanning supercontinuum reported in Sec. IV, we utilize an argon-filled hollow-core fiber as the light source. In all experiments, pulse compression is implemented by the pulse shaper for residual spectral phase compensation. To this end, the integrated second harmonic signal of the laser pulse is maximized using an evolutionary optimization algorithm [36,37]. The optical axes of the two liquid crystal displays (LCDs) A and B are oriented orthogonally at $\phi = \pm 45^\circ$. Applying linear spectral phases

$$\varphi_{A/B} = \mp\frac{\tau}{2}(\omega - \omega_0) \tag{11}$$

to LCD A and LCD B, respectively, generates an orthogonal linearly polarized (OLP) pulse sequence with a temporal separation of τ [12,16,34]. An achromatic quarter-wave plate (QWP) with horizontally aligned optical axis transforms the OLP sequence into a CRCP pulse sequence. Depending on the sign of τ, the resulting pulse sequence is either RLCP ($\tau > 0$) or LRCP ($\tau < 0$). Note that the subsequent half-wave plate (HWP) inverts the helicity. The CRCP pulse sequences are focused by a lens with a focal length of 250 mm into the interaction region of a velocity map imaging (VMI) spectrometer, to interact with potassium atoms in the gas phase provided by a dispenser source at a background pressure of about 5e-7mbar. Photoelectron wave packets from REMPI of potassium atoms triggered by the CRCP pulse sequence are projected onto a multichannel plate (MCP) detector in chevron configuration equipped with a phosphor screen which is imaged by a charge coupled device (CCD) camera. To obtain the full three-dimensional (3D) electron momentum distribution (3D-ED) from the measured projected electron momentum distributions (PED), we employed a tomographic technique [38–41]. In contrast to Abel inversion techniques such as the pBASEX algorithm [42], photoelectron tomography does not require any symmetry properties of the wave packet to be reconstructed and is therefore suitable to reconstruct vortex-shaped 3D-EDs. Since the ionizing laser pulse defines the orientation of the released 3D-ED, rotation of the laser pulse about its propagation axis using an achromatic HWP allows us to image the 3D-ED under different angles. From the PEDs obtained under 45 different angles between -90° and 86°, we retrieve the 3D-ED applying the Fourier slice algorithm [43]. An advantage of the Fourier slice algorithm compared to other reconstruction methods, such as the back projection algorithm, is that the angular discretization inherent to the measurement manifests in the Fourier domain rather than in real space. Therefore, the angular discretization is not palpable in the reconstructed 3D-ED.

Radial conversion of the electron vortices from the momentum to a kinetic-energy representation is performed by taking 151 2D slices through the reconstructed 3D-ED under different angles, performing a 2D calibration of each slice, and recombining the calibrated slices to obtain the energy-resolved 3D-ED. We estimate the energy resolution of the 3D-EDs to be better than 80 meV at a photoelectron kinetic energy of 1 eV.

Introducing a *relative* phase between the two pulses in the CRCP sequence provides an alternative, shaper-based approach to perform the spatial rotation of the CRCP sequence as required for the tomography, without using a HWP. To this end, a constant phase of $+\phi$ is applied to the LCP pulse, whereas a phase of $-\phi$ is applied to the RCP pulse to rotate the whole CRCP pulse sequence about an angle of ϕ. As a consequence, the electron vortex is rotated about ϕ. Mathematically, this is rationalized by considering the eigenvalues and eigenvectors of the rotation matrix $\boldsymbol{R}(\phi)$,

$$\boldsymbol{R}(\phi)\mathbf{e}_q = e^{qi\phi}\mathbf{e}_q, \tag{12}$$

where $\mathbf{e}_q$ describe the Jones vectors for LCP ($q = 1$) and RCP ($q = -1$) light. Accordingly, applying the rotation matrix to a CRCP pulse sequence reads

$$\boldsymbol{R}(\phi)(\mathbf{e}_1\mathcal{E}_L + \mathbf{e}_{-1}\mathcal{E}_R) = \mathbf{e}_1\mathcal{E}_L e^{i\phi} + \mathbf{e}_{-1}\mathcal{E}_R e^{-i\phi}. \tag{13}$$

Here, $\mathcal{E}_L$ and $\mathcal{E}_R$ describe the time-delayed envelopes of the LCP and RCP light pulses, respectively. It is seen that the *relative* phase of 2ϕ rotates the CRCP pulse sequence by an angle of ϕ. This technique is particularly advantageous for ultrabroadband pulses since the HWP is not required for pulse rotation.

IV. RESULTS AND DISCUSSION

In this section, we present our experimental results in three parts. In the first part (Sec. IV A), we study control of the radial vortex shape by variation of the time delay τ, including reversal of the pulse ordering, and the spectral bandwidth. In the second part (Secs. IV B 1 and IV B 2), we utilize neutral π-pulse excitation and continuum-continuum transitions to manipulate the azimuthal vortex shape. Finally, in the third part (Sec. IV B 3), we discuss manipulation of the vortex shape in the polar direction. Analysis of the relative phase of interfering wave packets with different $|m|$ allows us to reconstruct a free-electron wave function.

A. Control of the radial vortex shape

1. Amplifier spectrum

We start the discussion in the perturbative regime, where 1+2 REMPI results in a vortex with c_6 symmetry as described by Eq. (4). The first experiment was performed using $\Delta t = 20$fs pulses from the amplifier of our laser system. The choice of the time delay between the two pulses in the CRCP sequence is a trade-off between maximizing the pulse separation in order to avoid significant photoelectron generation from the linearly polarized field in the overlapping time window, on the one hand, and maximizing the vortex arm separation in order to resolve interference fringes with the spectrometer, on the other hand. In the first experiment, the time delay was chosen as $\tau = 2\Delta t = 40$fs, which ensures sufficient temporal separation of the two pulses. The positive time delay corresponds to an RLCP pulse sequence. The resulting spacing of interference fringes in the photoelectron spectrum is $\delta E = h/\tau \approx 100$meV, well above the spectrometer resolution. Taking into account the spectral bandwidth $\Delta\omega \approx 2\pi c\Delta\lambda/\lambda_0^2 = 240\,\frac{\text{mrad}}{\text{fs}}$ of the laser pulse, the total width of the photoelectron spectrum from three-photon ionization is approximately $\Delta E = \sqrt{3}\hbar\Delta\omega = 274$meV. Hence, the chosen time delay corresponds to about $\Delta E/\delta E \approx 2.7$ visible fringes in the photoelectron spectrum.

The 3D-ED obtained by tomographic reconstruction and energy conversion of the measured data is depicted in Fig. 3(a). For better visibility of the vortex structure, we enhanced the salient c_6 Fourier component [12]. In accordance with Eq. (4), the 3D-ED created by the RLCP pulse sequence displays a six-arm vortex with counterclockwise sense of rotation. In the top row of Fig. 4, the slice through the x-y plane of the 3D-ED is shown in (a) Cartesian and (b) polar representation. The radial distribution $\mathcal{R}_3^2(E)$ of the Archimedean spiral integrated over all angles ϕ essentially reflects the three-photon power spectral density of each laser pulse. In polar coordinates, the vortex arms evolve linearly along $E_n(\phi)$ curves predicted by Eq. (5) (black dashed lines). The negative slope of the spiral arms indicates the left-handed rotation of the electron vortex. The energy separation between adjacent arms is $\delta E = 0.1$eV in accordance with theoretical value $\delta E = \frac{h}{\tau}$. Overall, comparison between the calculated $E_n(\phi)$ curves and the measured vortex arms reveals excellent agreement between theory and experiment. As confirmed by our numerical simulations [44], the inhomogeneity of the vortex arms in the ϕ direction results from minor contributions of the $|p,-1\rangle$ state. This resonant intermediate state is populated perturbatively by the initial RCP prepulse and probed by the LCP postpulse (cf. Fig. 1). The inhomogeneity of the vortex arms leads to the signal variations in the inner parts of the measured PEDs, presented in Figs. 5 and 6, which arise from the angle-dependent integration over vortex arms with slightly different electron density.

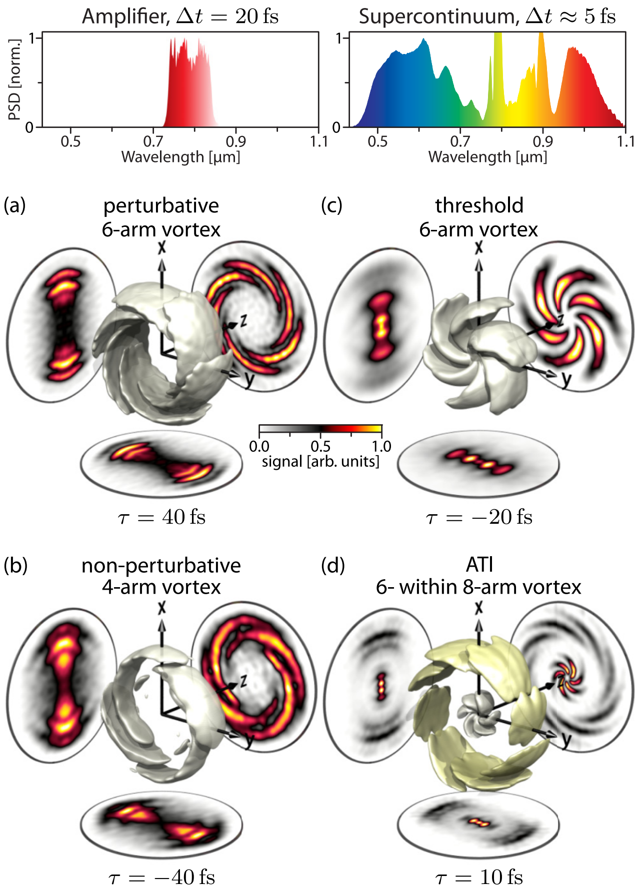

FIG. 3. Tomographically reconstructed electron wave packets $|\Psi(E,\vartheta,\phi)|^2$. The left column displays electron vortices generated by CRCP sequences of $\Delta t = 20$fs pulses from the laser system (spectrum shown on top). (a) Perturbative 1+2 REMPI using an RLCP sequence leads to the generation of a six-arm vortex with counterclockwise sense of rotation. (b) Nonperturbative ionization using an LRCP sequence of two π pulses changes the rotational symmetry to c_4 and reverses the rotational sense. The right column displays electron vortices generated by CRCP sequences of $\Delta t \approx 5$fs supercontinuum pulses (top frame). Due to the increased spectral bandwidth, the six-arm vortex from perturbative 1+2 REMPI extends down to the ionization threshold. Absorption of an additional photon in the continuum (ATI) gives rise to the eight-arm vortex shown in (d).

2. White-light supercontinuum

Next, we focus on the creation of electron vortices by REMPI with few-cycle CRCP pulse sequences. The supercontinuum input pulses from the hollow-core fiber compressor have a pulse duration of about $\Delta t = 7$fs and a spectral width of $\Delta E = 450$meV. The use of ultrabroadband laser pulses significantly extends the radial, i.e., kinetic-energy, distribution $\mathcal{R}_3^2(E) = \sqrt{3}\Delta E$ of the photoelectron wave packet. Using shorter time delays τ increases the fringe separation in the photoelectron spectrum. As an example, we present a perturbative electron vortex with c_6 symmetry, created by an LRCP supercontinuum pulse sequence with negative time delay of $\tau = -20$ fs, in Fig. 5. The figure displays a subset of 9 out of the 45 measured PEDs in angular steps of $\Delta\phi = 20°$. In comparison to the PEDs measured with the amplifier and presented in [12], the influence of both the enhanced spectral bandwidth and the shorter time delay is clearly discernible. The former results in the broadened photoelectron energy distribution extending down to the zero kinetic energy. The latter results in a higher fringe resolution due to the increased fringe separation of $\delta E = h/\tau \approx 200$ meV, corresponding to about $\sqrt{3}\Delta E/\delta E \approx 3.9$ visible fringes in the spectrum. To guide the eye, three arrows are added at fixed energies in the first row and column of Fig. 5. Following the evolution of the

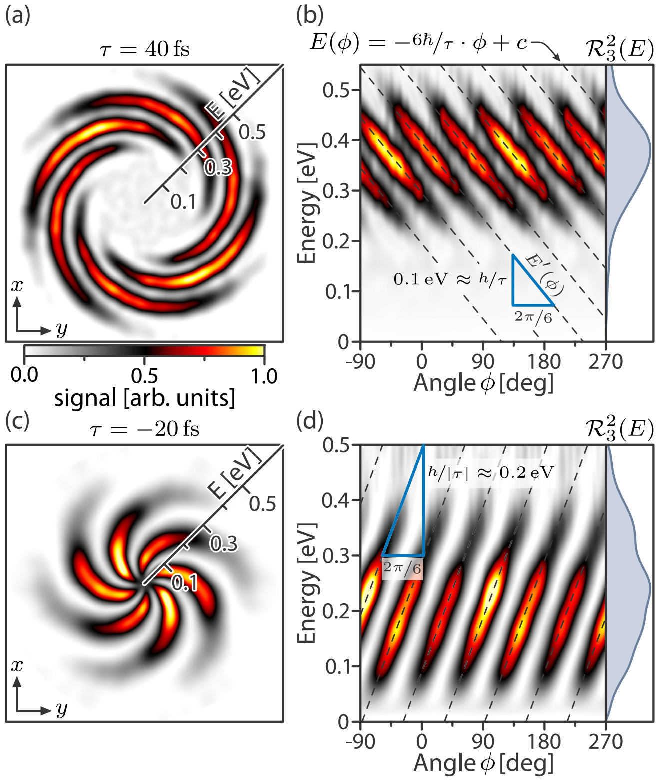

FIG. 4. Slices through the x-y plane of the six-arm electron vortex generated by (a) an RLCP sequence of $\Delta t = 20$fs pulses from the laser system and (c) an LRCP sequence of ultrabroadband supercontinuum pulses. In polar representation, displayed in (b) and (d), the vortex arms form straight lines with a slope of $-6\hbar/\tau$. The sign of the slope reflects the rotational sense of the vortices determined by the pulse ordering. Angle-integrated photoelectron spectra $\mathcal{R}_3^2(E)$ are plotted in the right-hand frames of (b) and (d). The x-y-coordinate axes in (a) and (c) indicate the orientation.

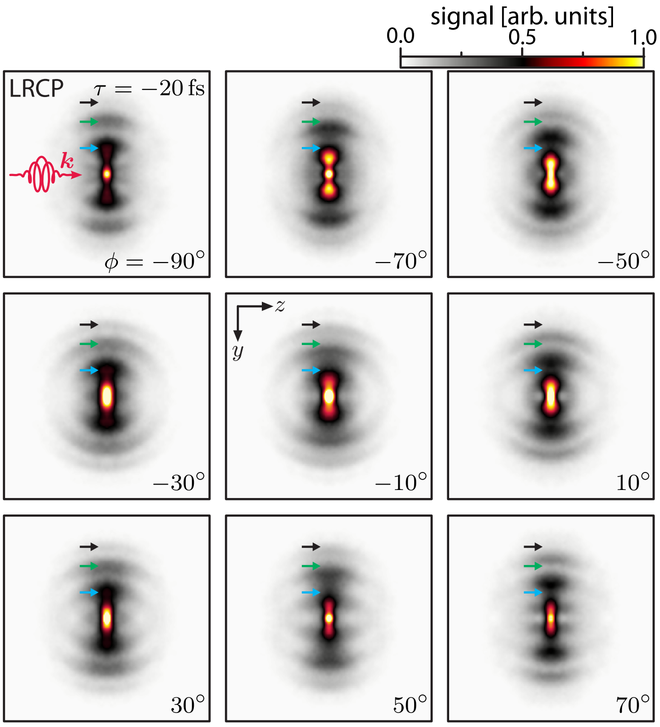

FIG. 5. Measured PEDs for different rotation angles ϕ of an LRCP supercontinuum pulse sequence. Arrows highlight the position of interference fringes observed in the y direction at $\phi = -90°$ (first frame). Comparison of PEDs in each row indicates that the fringes shift inwards under the clockwise rotation of the 3D-ED. Due to the c_6 symmetry of the electron vortex, the interference pattern recurs every $\Delta\phi = 60°$. Therefore, fringe positions of PEDs in the same column are identical. The y-z-coordinate axes in the central frame indicate the orientation.

fringe positions relative to the arrows along each row shows that the fringes shift inwards, i.e., towards lower energies, as expected for the clockwise rotation of an electron vortex with clockwise rotational sense. Because of the c_6 symmetry of the vortex-shaped wave packet, the fringe pattern recurs after $\Delta\phi = 60°$ rotation, which is confirmed by comparison of the PEDs displayed in each column.

The reconstructed 3D-ED depicted in Fig. 3(c) shows a six-arm electron vortex rotating clockwise due to the negative time delay. A slice through the x-y plane of the white-light vortex is shown in Figs. 4(c) and 4(d) in Cartesian and polar representation, respectively. The radial distribution extends down to the ionization threshold. Because the time delay is reduced by half, the energy separation of the adjacent vortex arms is twice as large as in the case of the amplifier spectrum shown in Figs. 4(a) and 4(b). In accordance with Eq. (5) for $\tau < 0$ (LRCP case), the vortex arms evolve linearly with a positive slope in the polar frame. Again, the calculated $E(\phi)$ curves in Fig. 4(d) coincide with the data.

B. Control of the azimuthal and polar vortex shape

Two different schemes to control the azimuthal shape, i.e., the rotational symmetry of the electron vortex, are investigated. In the first scheme, we make use of ATI and show experimentally that absorption of another photon in the continuum leads to an electron vortex with c_8 rotational symmetry. The second scheme is based on nonperturbative neutral excitation using a CRCP π-pulse sequence. We show that manipulation of the three-photon ionization pathways by populating the intermediate $4p$ state results in c_4 symmetry of the electron vortex.

1. Eight-arm vortex in the above-threshold ionization

The ATI scheme is implemented using a pair of white-light supercontinuum pulses with a duration of $\Delta t = 5$ fs and spectral bandwidth of $\Delta E = 632$ meV. The reduced pulse duration allowed us to decrease the time delay in an RLCP sequence even further to $\tau = 10$fs. The resulting energy separation of the vortex arms is $\delta E \approx 0.4$eV, which corresponds to about $\sqrt{3}\Delta E/\delta E \approx 2.7$ visible fringes in the energy distribution of threshold photoelectrons. Figure 6 shows a subset of measured PEDs for different rotation angles of the RLCP sequence. In order to increase the visibility of the interference pattern in the ATI, the total ATI signal is scaled by a factor of 3 and the c_8 Fourier component is slightly enhanced. Similar to Fig. 5, the first two columns display PEDs in angular steps of $\Delta\phi = 60°$. Accordingly, the fringe pattern of the threshold electrons recurs throughout

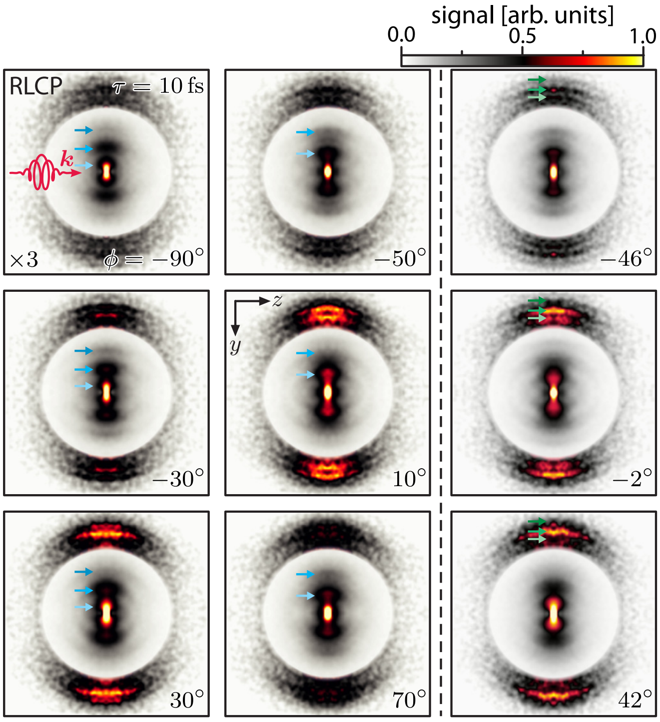

FIG. 6. Measured PEDs for different rotation angles ϕ of an RLCP supercontinuum pulse sequence including ATI. For better visibility, the overall ATI signal is scaled by a factor of 3. Blue and green arrows highlight the fringe positions in the threshold and ATI signal, respectively. The blue arrows (first and second column) are locked to the fringe positions, indicating their outwards shift under the clockwise rotation of the 3D-ED. The angular intervals $\Delta\phi$ were chosen such that the interference pattern recurs for all PEDs of the same column. For the six-arm vortex from threshold ionization, the pattern reappears every $\Delta\phi = 60°$ (left two columns). The fringe pattern of the eight-arm vortex in the ATI reappears every $\Delta\phi = 45°$ with varying intensity (right column). The y-z-coordinate axes in the central frame indicate the orientation.

each of the two columns, as indicated by the blue arrows. Under clockwise rotation of the 3D-ED (increasing ϕ), the fringes shift outwards, i.e., towards higher energies, indicating counterclockwise rotation of the underlying six-arm electron vortex. The fringe pattern in the ATI, on the other hand, is expected to recur every $\Delta\phi = 45°$ due to the c_8 rotational symmetry. Since the PEDs are acquired with an angular step size of $\Delta\phi = 4°$, the third column displays PEDs in angular steps of $\Delta\phi = 44°$. Indeed, the fringe position remains fixed throughout the third column, as indicated by the green arrows.

After tomographic reconstruction and enhancement of the salient c_8 Fourier component, we obtain the 3D-ED shown in Fig. 3(d). Besides the six-arm electron vortex from threshold ionization, the eight-arm vortex in the ATI is clearly visible. Both vortices display a counterclockwise sense of rotation in accordance with the positive time delay. The slice through the x-y plane of the 3D-ED is shown in Fig. 7 in (a) Cartesian and (b) polar coordinates. The ATI signal appears more pronounced in the polar representation due to scaling by the area element $d\mathcal{A} = E\,dE\,d\phi$. The energy separation of the spiral arms is the same for both the six-arm and the eight-arm vortex, being solely determined by the time delay τ.

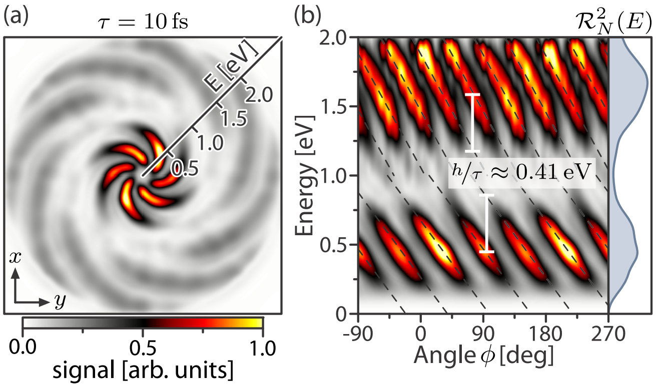

FIG. 7. Slice through the x-y plane of the free-electron wave packet created by an RLCP supercontinuum pulse sequence with a time delay of $\tau = 10$fs via 1+2 REMPI and ATI in (a) Cartesian and (b) polar representation. The inner vortex from threshold ionization exhibits c_6 rotational symmetry [cf. Figs. 3(c) and 4(c)], whereas the outer vortex resulting from ATI exhibits c_8 rotational symmetry. The x-y-coordinate axes in (a) indicate the orientation.

2. *Four-arm vortex from nonperturbative π-pulse excitation*

Next, we study control of the vortex symmetry by nonperturbative laser-atom interaction. Employing π pulses, with respect to the resonant $4s \rightarrow 4p$ transition, opens up a new ionization pathway leading to an $|f,-1\rangle$-type continuum, as displayed in Fig. 1(b). Interference of the $|f,3\rangle$ electron wave packet launched by the first pulse and the $|f,-1\rangle$ wave packet created by the time-delayed second pulse gives rise to a vortex with c_4 rotational symmetry. To demonstrate this scenario experimentally, we used an LRCP sequence of $\Delta t = 20$fs pulses from the laser system, with a time delay of $\tau = -40$fs. In the experiment, π-pulse excitation conditions were achieved by increasing the pulse energy by a factor of 4 relative to the perturbative scenario discussed in Sec. IV A 1. Slices through the reconstructed 3D-ED in the x-y plane ($\vartheta = 90°$) are shown in Figs. 8(a) and 8(b) in the Cartesian and the polar frame, respectively. In both representations, the c_4 rotational symmetry is clearly visible. The vortex arms again coincide with the linear $E(\phi)$ curves calculated using Eq. (10) and shown as black dashed lines in Fig. 8(b). The full tomographic reconstruction of the measured 3D-ED is presented in Fig. 3(b). For clarity of the illustration, only the central vortex containing the major part of the density is displayed. However, unlike the six- and eight-arm vortices discussed so far, the four-arm vortex results from a superposition of states with different $|m|$ [cf. Eq. (10)]. Therefore, the 3D-ED exhibits an additional modulation in the ϑ direction, which will be addressed in the following section.

3. *Reconstruction of the wave function*

The superposition of angular momentum states with different absolute value $|m|$ of the magnetic quantum number provides a means to measure the relative quantum mechanical phase of the wave function. Recently, we reported a measurement of the density of a pure $|f,-1\rangle$ free-electron wave packet [32]. Here, we extend these measurements by determining the phase of the $|f,-1\rangle$ wave packet using the

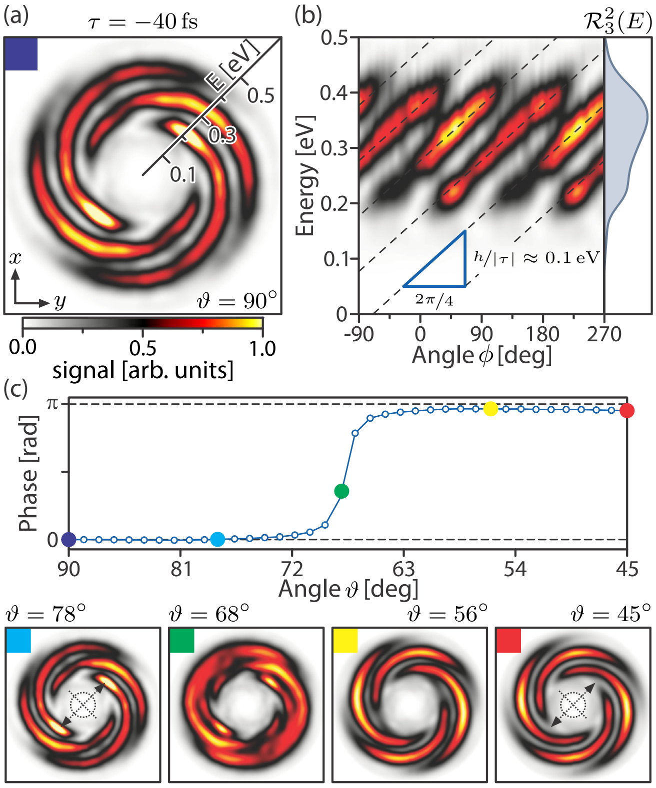

FIG. 8. Four-arm electron vortex from nonperturbative π-pulse excitation. (a), (b) Slices through the x-y plane ($\vartheta = 90^\circ$) of the 3D-ED in Cartesian and polar representation. (c) The retrieved quantum mechanical phase of the $|f,-1\rangle$ wave packet relative to the $|f,3\rangle$ reference wave packet as a function of the polar angle ϑ. The distinct π step observed in the c_4 vortex pattern around $\vartheta = 68^\circ$ is indicative of the node in the $|f,-1\rangle$ wave function. Slices through the 3D-ED taken at different ϑ close to the phase step are displayed in the bottom row. The crosshairs serve as a fixed reference to highlight the 45° rotation of the vortex pattern. The x-y-coordinate axes in (a) indicate the orientation.

$|f,3\rangle$ wave packet as a reference. Figure 8(c) shows the retrieved phase of the c_4 Fourier component as a function of the polar angle ϑ. Around $\vartheta = 68^\circ$, a distinct phase step of π is observed. According to Eq. (10), the phase shift is predicted to occur at $\vartheta = 63^\circ$ [see also Fig. 1(d)]. The deviation between theoretical model and experiment is explained by an additional contribution from a $|p,-1\rangle$-type ionization continuum, which is not included in the simplified theory presented in Sec. II. Additional interference between the corresponding torus-shaped wave packet $\psi_{p,-1}(E,\vartheta,\phi)$ and the vortex-shaped wave packet in Eq. (10) shifts the phase step to larger angles ϑ, i.e., towards the x-y plane. In our numerical simulations, we were able to reproduce the experimental finding using a relative mixing factor of the order of 0.5 for the $|p,-1\rangle$ contribution, in excellent accordance with [44]. The bottom row of Fig. 8(c) shows a series of slices through the 3D-ED, taken at various angles ϑ relative to the x-y slice shown in Fig. 8(a). The π-phase shift is expressed by the 45° rotation of the observed four-arm vortex pattern as the polar angle is scanned from $\vartheta < 68^\circ$ (yellow and red squares) to $\vartheta > 68^\circ$ (purple and blue squares). The slice taken at $\vartheta = 68^\circ$ (green square) marks the transition between both regions of the wave function. Here, the contrast of the vortex arms is strongly reduced and the angular distribution becomes nearly isotropic.

We found that the measured four-arm vortex displays the structure described by Eq. (10) in both the ϕ and ϑ directions. Indeed, we observe an Archimedean spiral with c_4 rotational symmetry with a π-phase step in the ϑ direction. As discussed in Sec. II, the interference of the $|f,-1\rangle$ wave packet with a reference wave packet allows direct measurement of the relative phase and therefore provides a different technique for the determination of atomic and molecular wave functions [45,46].

V. CONCLUSION AND OUTLOOK

In this paper, we report experimental results on the creation and control of 3D electron vortices obtained by multiphoton ionization of potassium atoms employing pairs of CRCP femtosecond laser pulses from white-light polarization shaping. The 3D electron vortices are reconstructed from multiple velocity map imaging measurements using a tomographic technique. In the perturbative regime, 1+2 REMPI leads to the generation of vortices with c_6 rotational symmetry. The use of ultrabroadband white-light supercontinuum pulses enabled efficient control over the radial, azimuthal, and polar shape of the vortex. Besides being able to measure the "full" vortex, i.e., an electron wave packet over a large range of photoelectron kinetic energies, the results feature high resolution of the interference fringes due to time delays down to 10fs. In addition, we observe an electron vortex with c_8 rotational symmetry in the above-threshold ionization (ATI). A vortex with c_4 symmetry is generated by nonperturbative neutral excitation. Evaluation of the relative phase of the interfering electron wave packets provides access to the relative quantum mechanical phase of the total free-electron wave packet, allowing direct measurement of the wave function rather than its probability density.

Currently, we study the generation of electron vortices with odd number of arms. As suggested by Eq. (8), such vortices arise from the interference of M- and N-photon pathways, with M and N being of opposite parity [13]. For the experimental implementation, we employ bichromatic fields from white-light polarization pulse shaping. In contrast to the $M = N$ case discussed in this contribution, the bichromatic M vs N scenario requires stabilization of the carrier envelope phase (CEP) of the laser field [16]. In addition, we plan to investigate strong-field effects in the electron vortices from nonperturbative ionization, including energy and phase shifts. Studying electron vortices of larger atoms will allow one to investigate electron-electron correlations in the multiphoton ionization of multielectron systems [47]. CRCP pulse sequences may also serve as a "bichiral" probe of the electron dynamics in the photoelectron circular dichroism (PECD) of chiral molecules [48,49].

ACKNOWLEDGMENT

Financial support by the Deutsche Forschungsgemeinschaft (DFG) via the priority program SPP1840 QUTIF is gratefully acknowledged.

[1] H. J. Lugt, *Vortex Flow in Nature and Technology*, 1st ed. (Wiley, New York, 1983).
[2] M. W. Scheeler, W. M. van Rees, H. Kedia, D. Kleckner, and W. T. M. Irvine, Science **357**, 487 (2017).
[3] M. Harris, C. A. Hill, and J. M. Vaughan, Opt. Commun. **106**, 161 (1994).
[4] P. Gregg, P. Kristensen, and S. Ramachandran, Optica **2**, 267 (2015).
[5] G. Spektor, D. Kilbane, K. Mahro, B. Frank, S. Ristok, L. Gal, P. Kahl, D. Podbiel, S. Mathias, H. Giessen, F. J. M. zu Heringdorf, M. Orenstein, and M. Aeschlimann, Science **355**, 1187 (2017).
[6] M. W. Zwierlein, J. R. Abo-Shaeer, A. Schirotzek, C. H. Schunck, and W. Ketterle, Nature (London) **435**, 1047 (2005).
[7] I. Bialynicki-Birula, Z. Bialynicka-Birula, and C. Sliwa, Phys. Rev. A **61**, 032110 (2000).
[8] J. H. Macek, J. B. Sternberg, S. Y. Ovchinnikov, T. G. Lee, and D. R. Schultz, Phys. Rev. Lett. **102**, 143201 (2009).
[9] S. Y. Ovchinnikov, J. B. Sternberg, J. H. Macek, T. G. Lee, and D. R. Schultz, Phys. Rev. Lett. **105**, 203005 (2010).
[10] L. P. H. Schmidt, C. Goihl, D. Metz, H. Schmidt-Bocking, R. Dörner, S. Y. Ovchinnikov, J. H. Macek, and D. R. Schultz, Phys. Rev. Lett. **112**, 083201 (2014).
[11] J. M. N. Djiokap, S. X. Hu, L. B. Madsen, N. L. Manakov, A. V. Meremianin, and A. F. Starace, Phys. Rev. Lett. **115**, 113004 (2015).
[12] D. Pengel, S. Kerbstadt, D. Johannmeyer, L. Englert, T. Bayer, and M. Wollenhaupt, Phys. Rev. Lett. **118**, 053003 (2017).
[13] J. M. N. Djiokap, A. V. Meremianin, N. L. Manakov, S. X. Hu, L. B. Madsen, and A. F. Starace, Phys. Rev. A **94**, 013408 (2016).
[14] K.-J. Yuan, S. Chelkowski, and A. D. Bandrauk, Phys. Rev. A **93**, 053425 (2016).
[15] K. J. Yuan, H. Z. Lu, and A. D. Bandrauk, J. Phys. B **50**, 124004 (2017).
[16] S. Kerbstadt, D. Timmer, L. Englert, T. Bayer, and M. Wollenhaupt, Opt. Express **25**, 12518 (2017).
[17] O. Tcherbakoff, E. Mevel, D. Descamps, J. Plumridge, and E. Constant, Phys. Rev. A **68**, 043804 (2003).
[18] B. Shan, S. Ghimire, and Z. Chang, J. Mod. Opt. **52**, 277 (2005).
[19] G. Sansone, E. Benedetti, F. Calegari, C. Vozzi, L. Avaldi, R. Flammini, L. Poletto, P. Villoresi, C. Altucci, R. Velotta, S. Stagira, S. De Silvestri, and M. Nisoli, Science **314**, 443 (2006).
[20] I. Barth and O. Smirnova, Phys. Rev. A **84**, 063415 (2011).
[21] T. Herath, L. Yan, S. K. Lee, and W. Li, Phys. Rev. Lett. **109**, 043004 (2012).
[22] M. Ilchen, N. Douguet, T. Mazza, A. J. Rafipoor, C. Callegari, P. Finetti, O. Plekan, K. C. Prince, A. Demidovich, C. Grazioli, L. Avaldi, P. Bolognesi, M. Coreno, M. Di Fraia, M. Devetta, Y. Ovcharenko, S. Düsterer, K. Ueda, K. Bartschat, A. N. Grum-Grzhimailo, A. V. Bozhevolnov, A. K. Kazansky, N. M. Kabachnik, and M. Meyer, Phys. Rev. Lett. **118**, 013002 (2017).
[23] P. Hockett, M. Wollenhaupt, and T. Baumert, J. Phys. B **48**, 214004 (2015).
[24] I. Georgescu, Nat. Phys. **11**, 800 (2015).
[25] M. Shapiro and P. Brumer, Rep. Prog. Phys. **66**, 859 (2003).
[26] J. Hübner, W. W. Rühle, M. Klude, D. Hommel, R. D. R. Bhat, J. E. Sipe, and H. M. van Driel, Phys. Rev. Lett. **90**, 216601 (2003).
[27] L. Costa, M. Betz, M. Spasenovic, A. D. Bristow, and H. M. Van Driel, Nat. Phys. **3**, 632 (2007).
[28] J. Güdde, M. Rohleder, T. Meier, S. W. Koch, and U. Höfer, Science **318**, 1287 (2007).
[29] D. Ray, F. He, S. De, W. Cao, H. Mashiko, P. Ranitovic, K. P. Singh, I. Znakovskaya, U. Thumm, G. G. Paulus, M. F. Kling, I. V. Litvinyuk, and C. L. Cocke, Phys. Rev. Lett. **103**, 223201 (2009).
[30] M. Förster, T. Paschen, M. Krüger, C. Lemell, G. Wachter, F. Libisch, T. Madlener, J. Burgdörfer, and P. Hommelhoff, Phys. Rev. Lett. **117**, 217601 (2016).
[31] D. Meshulach and Y. Silberberg, Phys. Rev. A **60**, 1287 (1999).
[32] S. Kerbstadt, D. Pengel, D. Johannmeyer, L. Englert, T. Bayer, and M. Wollenhaupt, New J. Phys. **19**, 103017 (2017).
[33] T. Brixner and G. Gerber, Opt. Lett. **26**, 557 (2001).
[34] J. Köhler, M. Wollenhaupt, T. Bayer, C. Sarpe, and T. Baumert, Opt. Express **19**, 11638 (2011).
[35] S. Kerbstadt, L. Englert, T. Bayer, and M. Wollenhaupt, J. Mod. Opt. **64**, 1010 (2017).
[36] T. Baumert, T. Brixner, V. Seyfried, M. Strehle, and G. Gerber, Appl. Phys. B **65**, 779 (1997).
[37] D. Yelin, D. Meshulach, and Y. Silberberg, Opt. Lett. **22**, 1793 (1997).
[38] M. Wollenhaupt, M. Krug, J. Köhler, T. Bayer, C. Sarpe-Tudoran, and T. Baumert, Appl. Phys. B **95**, 647 (2009).
[39] C. Smeenk, L. Arissian, A. Staude, D. M. Villeneuve, and P. B. Corkum, J. Phys. B **42**, 185402 (2009).
[40] M. Wollenhaupt, C. Lux, M. Krug, and T. Baumert, Chem. Phys. Chem. **14**, 1341 (2013).
[41] P. Hockett, M. Staniforth, and K. L. Reid, Mol. Phys. **108**, 1045 (2010).
[42] G. A. Garcia, L. Nahon, and I. Powis, Rev. Sci. Instrum. **75**, 4989 (2004).
[43] A. C. Kak and M. Slaney, *Principles of Computerized Tomographic Imaging* (IEEE Press, New York, 1988), pp. 1–339.
[44] P. Hockett, M. Wollenhaupt, C. Lux, and T. Baumert, Phys. Rev. Lett. **112**, 223001 (2014).
[45] J. Mauritsson, T. Remetter, M. Swoboda, K. Klünder, A. L'Huillier, K. J. Schafer, O. Ghafur, F. Kelkensberg, W. Siu, P. Johnsson, M. J. J. Vrakking, I. Znakovskaya, T. Uphues, S. Zherebtsov, M. F. Kling, F. Lépine, E. Benedetti, F. Ferrari, G. Sansone, and M. Nisoli, Phys. Rev. Lett. **105**, 053001 (2010).
[46] D. M. Villeneuve, P. Hockett, M. J. J. Vrakking, and H. Niikura, Science **356**, 1150 (2017).
[47] J. M. N. Djiokap, A. V. Meremianin, N. L. Manakov, S. X. Hu, L. B. Madsen, and A. F. Starace, Phys. Rev. A **96**, 013405 (2017).
[48] I. Powis, S. Daly, M. Tia, B. C. de Miranda, G. A. Garcia, and L. Nahon, Phys. Chem. Chem. Phys. **16**, 467 (2014).
[49] C. Lux, M. Wollenhaupt, T. Bolze, Q. Liang, J. Köhler, C. Sarpe, and T. Baumert, Angew. Chem., Int. Ed. Engl. **51**, 5001 (2012).